Revision #1

Ab initio DFT investigation of structural and vibrational properties of type B and mixed A-B carbonated hydroxylapatite.

Gianfranco Ulian[a], Giovanni Valdrè[a], Marta Corno[b], Piero Ugliengo[b]

[a] *Centro di Ricerche Interdisciplinari di Biomineralogia, Cristallografia e Biomateriali, Dipartimento di Scienze Biologiche, Geologiche e Ambientali Università di Bologna "Alma Mater Studiorum" Piazza di Porta San Donato 1, Bologna, Italy. E-mail: giovanni.valdre@unibo.it; Tel:+390512094943*

[b] *Dipartimento di Chimica and NIS Centre of Excellence, University of Torino, Via P. Giuria 7, 10125 Torino, Italy*

Abstract

In nature hydroxylapatite [$Ca_{10}(PO_4)_6(OH)_2$] is mostly present with various stoichiometric defects. The most abundant is the carbonate ion that can occupy different crystallographic sites (namely A and B types), however its effects on the apatite structure is still object of debate.

Type A carbonated apatite was quantum mechanically simulated in a previous study, here we extend the simulation to bulk structural and vibrational features of Na-bearing type B and mixed type A-B carbonated hydroxylapatite [$Ca_{10-x}Na_x(PO_4)_{6-x}(CO_3)_{x+y}(OH)_{2(1-y)}$, space group P1]. The simulation has been performed by *ab initio* density functional methods. The geometry of the models (lattice parameters and internal coordinates) have been fully optimized exploring different positions of the sodium ion in the apatite unit-cell. The results, in agreement with XRD data, suggest that in each crystallographic cell in the biological mineral there is at least one calcium ion substitution or vacancy per cell. The carbonate ion presence in the apatite structure is in good agreement with biological/chemical data. Furthermore, there is also a very good agreement with FTIR data reported in literature.

Keywords: type B carbonated hydroxylapatite, type A-B carbonated (hydroxyl)apatite, Structure, IR, Ab Initio DF, B3LYP

INTRODUCTION

Hydroxylapatite [$Ca_{10}(PO_4)_6(OH)_2$; OHAp] is commonly found in all igneous rocks and in some metamorphic and sedimentary ones and, also as the main component of the inorganic phase of bone, dentin and enamel tissues (Dorozhkin, 2009c). For this reason, apatite minerals draw the attention of many researchers not only in mineralogy, but also in biology, biochemistry and medicine. OHAp

is considered a key-biomaterial in cements and prosthetics for tissue repairing/reconstruction (Dorozhkin, 2009a; Dorozhkin, 2009b; Dorozhkin, 2009d).

In their first hierarchal level, biological hard tissues are characterized by the incorporation of minerals (inorganic phase) in a soft organic matrix of structural proteins, such as tropocollagen. The mineral phase is mainly given by hexagonal hydroxylapatite (space group $P6_3/m$), with parameters $a = b$ and a calcium channel where there are two hydroxyl groups oriented with the same direction along the *c*-axis. This polymorph is thermodynamically unstable if compared to the monoclinic phase (space group $P2_1/b$) typically found in rocks because of the proton order imposed by the same OH alignment in the apatite channel. The disorder/order transition have been evaluated at 200°C (Suda et al., 1995).

The biological hydroxylapatite is not a pure mineral, but presents vacancies and ionic inclusions/substitutions. The main substituting ion is the carbonate ion, with an average content of about 6% in weight. The carbonated hydroxylapatite (COHAp) accommodates the CO_3^{2-} ion either in place of both hydroxyl group in the *c*-axis channel of apatite (type A defect) or the phosphate group (type B) (Astala and Stott, 2005; Fleet, 2009; Fleet and Liu, 2007; Fleet and Liu, 2003; Fleet and Liu, 2004; Sturgeon and Brown, 2009; Suetsugu et al., 1998). The two types of defect usually coexist in a solid solution and the order of occurrence of A and B defects were extensively studied (Kovaleva et al., 2009). In recent years, the interest in those defective structures has increased, because it is known that chemical modification of OHAp, in particular the incorporation of carbonate ions, results in a considerable influence on the mineralization, demineralization and remineralization properties. Other properties, such as surface morphology and electrostatic potential, which influence interactions and adsorption processes at the mineral-organic interface in biological environment, could be affected by atomic substitutions, especially by the carbonate ion. Thus, obtaining accurate knowledge on the carbonate effects on both the apatite crystallographic cell and the surface leads to the possibility to design materials for prosthetic implants with

improved biomimetic and biocompatible properties (Gibson and Bonfield, 2002; Lafon et al., 2008; LeGeros, 2002).

Many experimental and theoretical studies were conducted on both type A and type B carbonated defect to better understand the role of the CO_3^{2-} ion on the structural variation and its spatial orientation within the OHAp cell (Astala and Stott, 2005; Engin and Girgin, 2009; Fleet and Liu, 2007; Fleet and Liu, 2008; Fleet and Liu, 2004; Fleet and Liu, 2005; Fleet et al., 2004; Gibson and Bonfield, 2002; Kovaleva et al., 2009; Peeters et al., 1997; Peroos et al., 2006; Rabone and de Leeuw, 2007; Suetsugu et al., 1998). Recently, we successfully investigated, by periodic quantum mechanics (QM) approach based on the hybrid B3LYP functional with an all electron basis set, the structural and vibrational features of type A fully carbonated apatite (CAp) (Ulian et al., 2013a; Ulian et al., 2013b). The results showed that the preferred CO_3^{2-} orientation in the cell is the "closed" configuration (A1), with a bisector of the triangular plane perpendicular to the *c*-axis, in good agreement with experimental data reported in literature (Fleet and Liu, 2003). In type B COHAp, it is known that the carbonate ion occupies one of the tetrahedron sloping faces of the substituted PO_4^{3-}. This substitution requires charge compensation, which can be obtained in several ways, such as the substitution of one of the calcium ion with a monovalent cation (sodium, potassium) or the inclusion of a small monovalent anion near the CO_3^{2-} (Peeros et al., 2006). The first example of coupled substitution is the most relevant, because Ca^{2+} ions can be easily substituted by both sodium and magnesium by 0.5 – 1.2 % wt. (Dorozhkin, 2009c), as it has been also experimentally observed in sodium-bearing apatites (Fleet and Liu, 2007). However, there is still some degree of disagreement on the effects of the substituent on the crystallographic cell parameters. Furthermore, the effect of the coupled mixed type A-B substitutions in the hexagonal OHAp cell is still unclear.

The aim of the present work is to complete the characterization of defective OHAp, considering type B and mixed type A-B defects. First we provide a detailed quantum mechanical (QM) analysis on the structural features of type B COHAp, adopting the same level of theory (B3LYP with all

electron basis set) and computational parameters used for type A CAp. Then, we extended the modelling to type A-B carbonated hydroxylapatite, using the results obtained from the separated A1 and B substitutions. Finally, the structural results were used provide the simulated phonon properties of type A and type B carbonate ions in both B-COHAp and mixed A-B C(OH)Ap to further investigate the differences between defective carbonated hydroxylapatite and a fully carbonated one.

COMPUTATIONAL DETAILS

All simulations have been made on a Debian Cluster with 40 cores adopting the periodic *ab initio* CRYSTAL09 code (Dovesi et al., 2009). With this software it is possible to study periodic systems by the implemented Hartree–Fock and Kohn–Sham self-consistent field (SCF) method. The pictures of the structures and their inspections have been carried out with the molecular graphic software MOLDRAW (Ugliengo et al., 1993) and VESTA (Momma and Izumi, 2008).

Basis set

Multi electron wave functions are described by linear combination of crystalline orbitals (CO), expanded in terms of Gaussian-type basis sets. For all the calculations, calcium has been described with a 86-511G(2d), used by other authors for calcite (Valenzano et al., 2006) and by us in our previous work (Ulian et al., 2013a, 2013b), with outer shell exponents α_{sp} = 0.453 bohr^{-2}, α_{d1} = 3.1910 and 0.8683 bohr^{-2} and α_{d2} = 0.2891 bohr^{-2}. The phosphorus atom is described by the basis 85-21G(d), α_{sp} = 0.48105 and 0.135 bohr^{-2} and α_{d} = 0.74583 bohr^{-2}, respectively. For the sodium atom, an 8-511G basis set was used (Dovesi et al., 1991). Oxygen and hydrogen are both represented by a 6-31G* basis set with the outer shell exponents α_{sp} = 0.2742 bohr^{-2} and α_{d} = 0.538 bohr^{-2}; and α_{sp} = 0.1613 and α_{p} = 1.1 bohr^{-2}, respectively. Finally, the carbon atom is described by a 6-21G* basis set with α_{sp} = 0.26 bohr^{-2} and α_{d} = 0.8 bohr^{-2} (Catti et al., 1993).

Hamiltonian and computational parameters

The Becke three-parameter (B3LYP) hybrid exchange functional (Becke, 1993) in combination with the gradient-corrected correlation functional of Lee, Yang, and Parr (Lee et al., 1988) has been adopted for all calculations. This functional has been already used for alkali oxides, α-quartz, calcite and hydroxylapatite (Dovesi et al., 1991; Pascale et al., 2005; Prencipe et al., 2004; Ulian et al., 2013a; Ulian et al., 2013b). The presence of some fraction of exact exchange increases the electronic localization, which in turn increases the ionic nature of the materials, causing a systematic decrease of the lattice parameters and an increase of the elastic constants and bulk moduli (Cora et al., 2004). The exchange–correlation contribution is performed over a grid of points and is the result of a numerical integration of the electron density and its gradient. The adopted pruned grid is given by 75 points and 974 angular points (75, 974-XLGRID), obtained from the Gauss–Legendre quadrature and Lebedev schemes (Prencipe et al., 2004). This is a good compromise between accuracy and cost of calculation for geometry optimization and vibrational frequencies. The values of the tolerances that control the Coulomb and exchange series are the default provided by CRYSTAL09 (*ITOL1* to *ITOL4* = 6) (Dovesi et al., 2009), but we increased the pseudo-overlap parameter (*ITOL5*) from 12 to 14. The Hamiltonian matrix has been diagonalized (Monkhorst and Pack, 1976) using a shrinking factor (*IS*) = 4. The same conditions have been adopted in our previous work on type A hydroxylapatite (Ulian et al., 2013a, 2013b).

Geometry

The geometry of the OHAp base-model used in this work was optimized within the $P6_3$ space group. For more details we suggest to refer to the paper of Ulian et al. (2013a). When carbonate ion defects were introduced in the structure, the subsequent optimization were carried without any symmetry constrain (*P1* symmetry).

Lattice constants and internal coordinates have been optimized within the same run using the analytical gradient method for the atomic positions and a numerical gradient for the unit-cell parameters. The Hessian matrix is upgraded with the Broyden–Fletcher–Goldfarb–Shanno algorithm. The tolerances for the maximum allowed gradient of the internal forces and the maximum atomic displacement for considering the geometry as converged have been set to 0.00006 hartree bohr^{-1} and 0.00012 bohr, respectively.

Phonon calculations

In periodic systems and within the harmonic approximation, the phonon frequencies at Γ point are evaluated diagonalising the central zone ($k = 0$) mass-weighted Hessian matrix:

$$W_{ij}(k=0) = \sum_G \frac{H_{ij}^{0G}}{\sqrt{M_i M_j}}$$

H_{ij}^{0G} is the second derivative of the electronic and nuclear repulsion energy E evaluated at equilibrium **u=0** with respect to the displacement of atom A in cell 0 ($u_i = x_i - x_i^*$) and displacement of atom B in cell G ($u_j = x_j - x_j^*$) from their equilibrium position x_i^*, x_j^*:

$$\sum_G H_{ij}^{0G} = \sum_G \left[\frac{\partial^2 E}{\partial u_i^0 \partial u_j^G} \right]_0 \qquad i = 1,...,3N; \quad j = 1,...,3N$$

In CRYSTAL, the calculation of the Hessian at equilibrium is made by the analytical evaluation of the energy first derivatives, Φ_j of E with respect to the atomic displacements:

$$\Phi_j = \sum_G v_j^G = \sum_G \frac{\partial E}{\partial u_j^G} \qquad j = 1,...,3N$$

while second derivatives at **u = 0** (where all first derivatives are zero) are calculated numerically using a "two-point" formula:

$$\left[\frac{\partial \Phi_j}{\partial u_i^0}\right]_0 \approx \frac{\Phi_j\left(0,...,u_i^0,...,0\right) - \Phi_j\left(0,...,u_i^0,...,0\right)}{u_i^0} \qquad (156)$$

$$i = 1,...,3N; \quad j = 1,...,3N$$

More details on the vibrational calculation made by CRYSTAL can be found in literature (Pascale et al., 2004; Tosoni et al., 2005). The Hessian matrix eigenvalues provide the normal harmonic frequencies ω_h and it is obtained with 3N+1 SCF and gradient calculation.

Also, an anharmonic correction has been applied to the OH stretching mode in the type B COHAp cell. This three-step procedure is based on: (i) decoupling of the distance O–H, which is treated as a pure normal coordinate; (ii) calculation of the total energy of the system for a set of OH values around equilibrium (0.2/+0.3Å), followed by an interpolation by means of a sixth-order polynomial fit, and (iii) solution of the one-dimensional nuclear Schrödinger equation to obtain the three lowest eigenvalues, E_0, E_1 and E_2, from which one can calculate the fundamental frequency $\omega_{01} = E_1 - E_0$, the first overtone $\omega_{02} = E_2 - E_0$ and the anharmonicity constant of the OH mode, $\omega_e\chi_e = (2\,\omega_{01} - \omega_{02})/2$. This algorithm was proposed by Lindberg (Lindberg, 1988) and already adopted by other authors (Pascale et al., 2004; Ugliengo et al., 2004; Ulian et al., 2013b).

RESULTS AND DISCUSSION

Type B carbonated hydroxylapatite

In the type B defect formation in OHAp, the CO_3^{2-}/PO_4^{3-} substitution would lead to a positively charged cell. Many ways were proposed to restore the cell neutrality (Peroos et al., 2006), we chose the following charge balancing reaction:

$$PO_4^{3-}{}_{(cell)} + Ca^{2+}{}_{(cell)} + CO_3^{2-} + M^+ \rightarrow CO_3^{2-}{}_{(cell)} + M^+{}_{(cell)} + PO_4^{3-} + Ca^{2+} \qquad (175)$$

where a Ca^{2+} is substituted by a monovalent ion, that could be any one of the alkaline elements. In this work we have chosen the sodium ion ($M^+ = Na^+$) because it possess an ionic radius close to that of calcium and thus it is sterically comparable. In fact, sodium-bearing apatites have been

179 experimentally reported and were extensively studied by X-Ray Diffraction (XRD) and Fourier
180 Transform Infrared (FTIR) analysis (Fleet and Liu, 2007; Kovaleva et al., 2009).
181 The modelling of type B COHAp involved the geometrically optimized OHAp structure that we
182 have recently reported (Ulian et al., 2013a). Since there are six phosphate ions and ten calcium ions
183 in a crystallographic cell of hydroxylapatite (Fig. 1), the combined CO_3^{2-} and Na^+ substitution
184 would lead to 60 models which are compatible with type B defect. However, since all the PO_4^{3-} are
185 symmetry related within the *P6₃* space group, we fixed the CO_3^{2-}/PO_4^{3-} substitution on the P13
186 phosphate ion (see Fig. 1). This operation reduces the symmetry to of the OHAp cell to *P1*. In this
187 condition all the ten calcium ions are non-equivalent and a full analysis of the type B COHAp
188 structure required ten models, one for each Ca/Na substitution.
189 Thus, the rationale of the model creation was the following: (i) starting from the pure OHAp we
190 removed the phosphate ion labelled as P13, (ii) then we placed the CO_3^{2-} on the bottom sloping face
191 of the removed tetrahedron and (iii) substituted a calcium with a sodium ion. Steps (i) and (ii) were
192 the same for each model, while (iii) involved each Ca^{2+}: this method allowed to reduce the number
193 of necessary models from 60 to just 10.
194 In Table 1 we reported the results of the geometrical optimization conducted on the type B COHAp
195 structures. According to the adopted computational parameters, all the presented data in this work
196 have an uncertainty on each atomic position of about 0.00006 Å. Because of the same atomic
197 composition, it was possible to directly compare the energy of the different models. The most stable
198 one presents the Na^+ replacing Ca6 ion (Na6 model, see Fig. 2b), followed by the Na2 model where
199 Na^+ replaces Ca2 ion, which differs energetically from Na6 model by just +1.45 kJ/mol (Fig. 2a).
200 The relative stability of the type B COHAp structure is probably due to a subtle interplay between
201 the CO_3^{2-} and Na^+ relative distances and the distortion of the hosting structure to accommodate for
202 the defect. In particular, the structure is stable when the sodium ion is in a position near to the
203 oxygen vacancies related to the phosphate substitution, as it is possible to see in the results in Table
204 1. This observation would prove the hypothesis proposed by Fleet and Liu (2007). The actual

energy values are high enough to conclude that only the Na2 and Na6 models exhibits significant populations in the absence of the thermal effects while all other cases are not present at room temperature.

Compared to our previous results of pure OHAp model (Ulian et al., 2013a), the combined CO_3^{2-} /Na^+ substitutions cause a contraction of the crystallographic cell along the *a*- and *b*-dimensions, while the *c*-axis expands slightly. We noticed that the Ca3 --- Ca3 interaction distances slightly decreased by about 0.1 Å, which means that the calcium channel was also contracted by about 2.0%. These results are solely due to the carbonate ion, which is smaller than the substituted phosphate ion. The Na^+ ionic radius is close to the Ca^{2+} one and, as also suggested by previous studies (Peroos et al., 2006), its effects on cell variation are negligible. Angular distortions of the lattice are predicted to be small for the most stable Na2 and Na6 configurations, they remain below 0.8 degrees as compared to the OHAp parent structure.

Although the lattice parameters variations, the type B carbonate ion did not valuably affects the crystalline framework. The PO_4^{3-} tetrahedrons in the unit-cell were only slightly rotated to accommodate the CO_3^{2-} ion, but these rotations were negligible if compared to those of type A defect (Ulian et al., 2013a). The mean P-O and O-H bond lengths are almost the same in each model and they are very close to the OHAp values. We observed a reduction of the O-H---O-H interaction distances from 2.41 Å to 1.99 Å and in the case of Na5, Na7 and Na8 models it leaded to the formation of a hydrogen bond between the two OH groups in the unit-cell.

In Fig. 3 we reported a section of the unit-cell involved in the PO_4^{3-}/CO_3^{2-} substitution. The highlighted phosphate tetrahedron face (Fig. 3a,c) represents the initial carbonate ion position. After the geometry optimization of the type B COHAp (Fig. 3b,d), we observed a rotation of the CO_3^{2-} molecular plane on the [001] and [110] directions by -15° and -46°, respectively (see Fig. 3). Although there were minimal positional or angular variations between the ten models, the local geometry showed in Fig. 3 was maintained. The observed carbonate ion position is in line with both previous theoretical studies made by molecular dynamics approach (Peroos et al., 2006) and

experimental XRD refinement (Fleet and Liu, 2007), where the same molecular canting was observed.

Compared to XRD refinements reported in literature (Fleet and Liu, 2004; Kovaleva et al., 2009; Yahia and Jemal, 2010), the type B COHAp resulting from our quantum mechanical simulations is in good agreement with experimental results. The differences on the crystallographic lattices are ±0.050Å on *a* and *b* cell parameters and +0.010 on the *c* one. Generally, the simulated type B carbonated hydroxylapatite unit-cell volume is slightly contracted than the experimental by about 3Å^3. This could be due to the presence also of type A carbonate or other defects in the experimental samples, as reported by the authors, and to the approximations in the quantum mechanical calculations.

Type A-B carbonated hydroxylapatite

In this section the focus is on the effect of coupled type A and B defects on the crystallographic cell of hydroxylapatite. We have considered various configurations and mutual distances of the defects in both a single cell and in a supercell.

Single-cell of type A-B carbonated apatite

We initially considered a single unit-cell of OHAp in which both type A and B carbonate ions are included, accordingly to the reactions:

$$2OH^-_{(cell)} + CO_3^{2-} \rightarrow (A1)CO_3^{2-}{}_{(cell)} + 2OH^-$$

$$PO_4^{3-}{}_{(cell)} + Ca^{2+}{}_{(cell)} + CO_3^{2-} + Na^+ \rightarrow (B)CO_3^{2-}{}_{(cell)} + Na^+{}_{(cell)} + PO_4^{3-} + Ca^{2+}$$

The resulting structure has chemical formula $Ca_9Na(PO_4)_5(CO_3)_2$, with a carbonate ion content of 12.3 wt.% and without any OH^- groups. The two models have been created with the same CO_3^{2-} positions in A and B sites but with sodium ion substituting Ca2 and Ca6 sites. This choice was made taking into account the previous results on the stability of type B COHAp. The orientation of the carbonate ion in the apatite channel (type A1) was selected as the same of that reported in a

257 previous work (Ulian et al., 2013a), which was the most stable one. The results of the optimization
258 are reported in Table 2.
259 The coupled substitution caused a small compression of the lattice parameters *a* and *b* and an
260 expansion of the *c* one. However, the contraction on the *a* and *b*-dimensions is smaller than the one
261 observed for the pure type B carbonated apatite: this is due to the type A carbonate ion in the
262 calcium channel, which causes an expansion on *a* and *b*-dimensions and this explains the observed
263 effect on the unit cell. The obtained values are in good agreement with the XRD data on a Na-
264 bearing type A-B COHAp sample with similar CO_3^{2-} content (Fleet and Liu, 2007). The bond
265 lengths and angles are not significantly different. During the geometry optimization process, the
266 type A1 CO_3^{2-} ion rotated counter-clockwise on its plane of about 180°, bringing the C – O bond
267 perpendicular to the [001] direction near the type B carbonate ion. It is worth noting that this
268 rotation brought the type A1 carbonate ion first in the A2 configuration, then after the optimization
269 again in A1 configuration. The model with Ca6/Na6 substitution is more stable than that with
270 Ca2/Na2. This result is in agreement with the data of the type B carbonate defect in apatites
271 reported in the previous section.
272
273 *Supercell of type A-B carbonated apatite*
274 The single cell of type A-B CAp described in the previous paragraph is a good starting point to
275 analyse the interaction between type A1 and type B carbonate ions. However, in that structure the
276 relative distances between the CO_3^{2-} ions is almost fixed to about 3 Å because of their contiguity
277 within the same unit-cell, which allows to study only their short-range interactions. It would be
278 interesting to study a case in which the defects are less close by adopting a supercell approach. The
279 adoption of the canonical unit cell forces the removal of all OH groups in order to accommodate the
280 mixed A-B type defects, while OH groups are experimentally found in both natural and synthetic
281 carbonated apatites.

In order to take into account the above mentioned considerations, i.e., both the non-contiguity of type A and type B defects and the experimental observations of the presence of the OH groups, we modelled a "supercell". We doubled the *a* and *b* cell parameters, obtaining a structure that was 2 x 2 x 1 the original one, with four unit-cells of OHAp and chemical formula $Ca_{40}(PO_4)_{24}(OH)_8$ (Fig. 4a). This larger model allowed to place the type A and B defects in different contiguous unit-cells, thus to consider different carbonate ions relative distances. To create the mixed A-B COHAp we initially made the type A1 CO_3^{2-} substitution: the four unit-cells are equivalent due to the symmetry of the supercell, so the choice is indifferent. The substitution resulted in a type A COHAp, a structure without any internal symmetry given by a solid solution of three OHAp unit-cells and a type A1 CAp one. Fixing this partial model, the type B carbonate ion could be placed in one of the three remaining hydroxylapatite unit-cells, thus defining three models that are:

(i) with the type B defect in the unit-cell contiguous to the type A1 CAp one along the *b*-axis (labelled as AB-1 in Fig. 4b);

(ii) with the type B defect placed along the *ab* diagonal (labelled as AB-2 in Fig. 4b);

(iii) with the type B defect placed along the *a*-axis (labelled as AB-3 in Fig. 4b).

In each model, the sodium ion of the type B defect always substituted a Ca6 ion in the unit-cell.

The resulting structures are then solid solutions of two OHAp, one type A1 CAp and one Na-bearing type B COHAp unit-cells, with chemical formula $Ca_{39}Na(PO_4)_{23}(CO_3)(OH)_6(CO_3)$ (normalized to $Ca_{9.75}Na_{0.25}(PO_4)_{5.75}(CO_3)_{0.25}(OH)_{1.5}(CO_3)_{0.25}$) and a carbonate ion content of 3.01 wt.%. The results have been reported in Table 3.

To ease the interpretation and in order to make a direct comparison with previous results and with XRD experimental data, the lattice parameters *a* and *b* have been normalized with respect to the models with type A and B defects in a single unit cell. The three models AB-1, AB-2 and AB-3 have CO_3 --- CO_3 distances that increase following the trend AB-3 < AB-1 < AB-2, where periodicity was also took into account. The type A1 carbonate ion in the first and second model rotates about the *c-axis* as to follow the type B CO_3^{2-} ion.

The average bond lengths and angles are almost unaffected by the different carbonate ions relative distances. However, it seems that the structure stability increases in the following order AB-1 > AB-3 > AB-2. This trend does not follow the CO_3 --- CO_3 distances as it has could be expected. At low distance (AB-3) there could be some direct coulomb repulsion between carbonate ions that decreased the structure stability. At high distance (AB-2) the instability is amplified, probably because of the lack of interaction. Then, the most stable structure must lie between these two limit distances considered. Given the relative small energy differences between the most favourable structures (AB-1 and AB-3), it may be suggested that the experimental structure refers to a "geometrical" mix of these two structures or, more precisely, of all structures that are within k_BT of the energetically most favourable structure, where k_B is the Boltzmann's constant and T is the temperature. As observed before, the coupled substitution caused a slight expansion of the *c* parameter, but the *a*- and *b*-dimensions showed different behaviours according to the type B defect location in the models. In particular, there is a full expansion along every lattice axis in the AB-1 model, which may explain its stability. The mean bond lengths and angles of the crystalline framework were not significantly affected. It is worth noting that provided XRD data are somehow incomplete and thus a full comparison between the interatomic distances and angles was not possible. However, we reported the crystallographic information framework (CIF) data files for all the structures obtained from our simulations, which were used to measure the internal geometry of the models, to help others in interpreting their results.

In general, all the structural results are in good agreement with the experimental data (see Table 4). The calculated lattice parameters show small variations between the different carbonated (hydroxyl)apatite models, with a larger deviation on the type A defective structure, but the evaluated data are consistent with experimental evidence. In each model but the single-cell type A-B CAp the calcium ion content is higher than the relative one in biological tissues, but in good agreement with that of synthetic apatites (Fleet and Liu, 2007). This is not surprising, because Ca^{2+} ions can be easily substituted by both sodium and magnesium by 0.5 – 1.2 % wt. (Dorozhkin,

2009c). Thus, the type A-B CAp model suggests that in each crystallographic cell in the biological mineral there is at least one calcium ion substitution or vacancy per cell. The phosphorus weight content is in line with the experimental data. In particular, it seems that in the bone tissue there is in average one type B defect per unit cell. On the other hand, the enamel has a higher P content than the other hard tissues, which suggests the presence of less type A and B carbonate ion in the structure. The carbonate ion presence in the apatite structure is in good agreement with biological/chemical data, with an exception for the single-cell type A-B CAp model. The Na^+ content is more represented by the type A-B supercell models, because in both type B COHAp and single-cell of mixed A-B CAp it is more than two times the experimental values.

Simulated infrared properties of carbonate ions

Type B carbonated hydroxylapatite

The type B COHAp unit-cell does not have internal symmetry, thus its (43 x 3) - 3 = 126 vibrational modes belong only to the A irreducible representation (IRREP):

$$\Gamma_{total} = 126\ A$$

The vibrational modes can be subdivided in three regions: lattice modes (< 400 cm-1), phosphate ion vibrations (500 – 1200 cm^{-1}) and carbonate ion modes (600 – 1800 cm^{-1}). In the following we discuss in details each vibrational region of the simulated type B COHAp spectrum.

FTIR and Raman spectra of the free phosphate tetrahedron in aqueous solution present four vibrational modes (irreducible representations A_1+E+2F): (i) the symmetric P-O stretching (ν_1, A_1) at 938 cm^{-1}; (ii) the symmetric OPO bending (ν_2, E) at 420 cm^{-1}, which are IR inactive; (iii) the asymmetric P-O stretching (ν_3, F) at 1017 cm^{-1} and (iv) the asymmetric OPO bending (ν_4, F) at 567 cm^{-1} (Corno et al., 2006; Rehman and Bonfield, 1997; Tsuda and Arends, 1994). When the PO_4^{3-} ion is in a molecular crystals, such as hydroxylapatite, the crystalline field induces distortions of the perfect phosphate tetrahedron, reducing its symmetry. In particular, within both type A and type B

359 defective COHAp structures the phosphate ion lies in a framework which does not have any
360 symmetry feature. This lead to the loss of degeneracy of the highly symmetric phonon modes and to
361 the activation of all the silent ones (B symmetry) previously described (Corno et al., 2006; Ulian et
362 al., 2013b), thus to the presence of more signals in the infrared spectra.
363 The spectrum presented in Fig. 5 is related to the Na6 model of type B COHAP, the most stable
364 structure obtained. The asymmetric phosphate ions, $\nu_3(PO_4)$, at 1022-1140 cm^{-1} stretching signal is
365 the most intense in the spectrum. This band is more complex than that of pure OHAp, because it is
366 composed by 18 active modes originated by the degeneracy loss of E_1 and E_2 vibrational modes.
367 Despite the complexity, the $\nu_3(PO_4)$ band in type B COHAp is very similar to that of OHAp, more
368 than that of type A CAp (Ulian et al., 2013b). The P-O symmetric stretching (ν_1) signal can be
369 found in the 876 – 977 cm^{-1} range, composed by six phonon modes. The OPO asymmetric (ν_4) and
370 symmetric (ν_2) bending modes are located in the 562 – 630 cm^{-1} (medium intensity) and 426 – 494
371 cm^{-1} (very low intensity) ranges, respectively. In general, the CO_3^{2-}/PO_4^{3-} substitution caused a
372 slight broadening of the phosphate vibrational band, leaving the high-intensity signal positions
373 almost unchanged: this means that the type B carbonate defect in OHAp interacts poorly with the
374 crystalline framework. Taking into account this consideration, the complete vibrational analysis has
375 been conducted only on the most stable type B COHAp model (Na6). Similar PO_4^{3-} phonon modes
376 in the other nine theoretical type B COHAp structures were assumed.
377 Regarding the hydroxyl groups, the O-H stretching mode falls at two different wavenumbers, 3774
378 cm^{-1} and 3759 cm^{-1}. The first signal is relative to the stretching of an hydroxyl group near to the
379 charge-balancing sodium ion at a distance of 2.35 Å. The other peak is very close to the O-H
380 signal of pure hydroxylapatite, at 3757 cm^{-1} (Ulian et al., 2013b). When anharmonicity was taken
381 into account (see the Computational Methods section), the two stretching modes shifted to lower
382 wavenumbers, at 3693 cm^{-1} and 3597 cm^{-1} respectively, in good agreement with the FTIR result of
383 Fleet and Liu (2007). The 500 – 700 cm^{-1} region of the type B COHAp spectrum has more signals

384 than that of type A CAp, because of the presence of eight OH libration modes. These phonon
385 signals concur in the formation of two peaks at 622 – 630 cm^{-1} (four modes of medium-intensity)
386 and 701 – 722 cm^{-1} (four modes of very-low intensity), close to the results obtained for pure
387 hydroxylapatite (an IR/Raman band at 636 cm^{-1}, E_1 symmetry, and the Raman signal at 724 cm^{-1}, E_2
388 symmetry). As we have reported in our previous work, OH libration are affected by anharmonicity
389 and, unfortunately, the CRYSTAL09 code allows to apply the correction only to the stretching ones
390 (Ulian et al., 2013b), preventing the direct comparison between the theoretical (with harmonic
391 approximation) and the experimental OH modes.

392 The free CO_3^{2-} in aqueous solution has four modes: asymmetric stretching (ν_3, *E'* symmetry),
393 symmetric stretching (ν_1, *A'*$_1$ symmetry). bending out-of-plane (ν_2, *A''* symmetry) and bending in
394 plane (ν_4, *E'* symmetry). In the IR spectrum, the the *A'*$_1$ symmetry mode relative to the symmetric
395 stretching is inactive, because it does not cause dipole variations. In the apatite framework, the
396 symmetry reduction causes the loss of degeneracy of *E'* modes, giving origin to two doublets and to
397 the activation of the symmetric stretching mode.

398 The characteristic carbonate bands in apatite lattice are the asymmetric stretching (ν_3) and the out-
399 of-plane bending (ν_2). The simulated peaks occurred in the Na6 model spectrum (Fig. 5) at 1481
400 and 1562 cm^{-1} for the ν_3 vibration and at 876 cm^{-1} for the ν_2 one. We compared the type B CO_3^{2-}
401 modes with those of the simulated type A1 CAp spectra reported in a previous paper (Ulian et al.,
402 2013b). The asymmetric stretch doublet of type B was at lower frequencies than that of type A1.
403 However, they maintained a similar separation (81 cm^{-1} in type B and 86 cm^{-1} in type A1). The
404 $\nu_2(CO_3)$ mode fell very close to the same band observed for the type A1 CAp (878 cm^{-1}).

405 The CO_3^{2-} vibrational modes in the other nine optimized models have been obtained separately with
406 the FRAGMENT keyword (Dovesi et al., 2009). The related spectra are reported in Fig. 6 and the
407 frequency values in Table 5. The carbonate asymmetric stretch doublets (ν_3) are at different
408 frequencies with respect to the Na6 model. A consistent comparison is possible using this method

because repeating the frequency calculation on the Na6 model with the FRAGMENT keyword returned almost the same values obtained with the full calculation. This result further confirms the low interaction of the type B carbonate ion with the crystalline framework. We observed a systematic red shift of the ν_{3b} signal, with different entity from one structure to another. The ν_3 band follow this trend in four cases (Na1, Na3, Na4 and Na8 models), but in the remnant structures it is blue shifted. In this latter case this leaded to a reduction of the doublet separation, which is very noticeable in Na5, Na9 and Na10 spectra. This effect was due to the different Ca^{2+}/Na^{+} substitutions in the unit-cell. Considering that in experimental samples the sodium ion occupies different positions simultaneously, this result could explain a significant band broadening of this mode ($\nu_{3max} - \nu_{3min} \approx 45$ cm^{-1}).

The $\nu_2(CO_3)$ band fell at almost the same frequency in each model (876 cm^{-1}), which means that the sodium ion position did not interfered with this vibrational mode. The symmetric stretching (ν_1) and the in-plane bending (ν_4) modes are also slightly affected by the different Na^{+} ion position, with the signals red shifted when compared to the Na6 model.

Type A-B carbonated (hydroxyl)apatite

In this section the focus is on the effects of the CO_3^{2-} --- CO_3^{2-} relative distance on the IR signal positions. The results are collected in Table 6.

Compared to the to the type A1 CAp simulated in a previous work (Ulian et al., 2013b), in the fully carbonated cell of type A1-B CAp all the signals but the ν_1 one are red shifted (Fig. 7a).

When the different solid solution of hydroxylapatite and carbonate defects were considered, we observed an inversion of the order of $\nu_{3a}(CO_3)$ modes at different CO_3^{2-} relative distances (Fig. 7b). When the two defects are very close, *i.e.* in the single unit-cell of type A-B CAp, there is first the ν_{3a}(A) mode, then the ν_{3a}(B) one (at 1442 and 1436 cm^{-1}, respectively); in type A-B COHAp, either AB-1, AB-2 and AB-3 models, the order is reversed (1470 cm^{-1} for ν_{3a}(B) and 1505 cm^{-1} for

434 ν_{3a}(B)). The order of occurrence of the $\nu_{3b}(CO_3)$ signal is not affected by the positions of the type A
435 and type B defect in the apatite cell. The out-of-plane bending (ν_2) falls almost at the same position
436 in the supercell models of type A-B carbonated hydroxylapatite.
437 Respect to both singly type A1 and type B defects, the symmetric stretching mode (ν_1) is slightly
438 red shifted ($\Delta\nu \approx 10$ cm^{-1}) in the AB-1, AB-2 and AB-3 models, while the effect is larger in the AB-
439 Na6 one ($\Delta\nu > 15$ cm^{-1}). In the type AB supercell models the carbonate ion modes are shifted to
440 different position, with no apparent behavior. In particular, the ν_2 signals can be quite well resolved
441 in AB-3 or slightly overlapped in AB-1 and AB-2 models.
442 We compared our phonon results with experimental Raman/FTIR analysis reported in literature
443 for a variety of samples (Table 7). Both natural and synthetic samples were experimentally
444 investigated (Fleet et al., 2011; Penel et al., 2005; Petra et al., 2005; Sturgeon and Brown, 2009;
445 Yahia and Jemal, 2010). There is a very good agreement on the $\nu_2(CO_3)$ mode to each simulated
446 structure, both with singly and coupled type A1 and type B defects, with only negligible variations
447 from +1 to +9 cm^{-1}. This is an important result, because the quantification of the carbonate content
448 in apatite is usually made from the intensity of the out-of-plane band and our approach adequately
449 describe this region of the spectrum. Differences are present in the asymmetric stretch region (1400-
450 1500 cm^{-1}). Our $\nu_3(CO_3)$ doublet for type B carbonate ion was blue shifted of about +70 cm^{-1} and
451 presented a larger separation between the two signals (81 cm^{-1}) than the experimental ones (~50 cm^{-}
452 ^{1}). This observation can be extended to type A1 ν_3 signals, but the difference from experimental
453 results is less than the one found for the type B phonon mode. The effect on the ν_3 modes could be
454 related to the adopted computational methods, since there is a systematic shift of the calculated
455 signals. A configuration where the CO_3^{2-} ion is placed in the Ca^{2+} channel with a bisector of the
456 carbonate triangular plane parallel to the **c**-axis (type A2) was reported (Fleet et al., 2011). It was
457 found by FTIR analysis an asymmetric stretching mode doublet relative to the A2 carbonate ion at
458 1569 and 1507 cm^{-1}. This CO_3^{2-} configuration was found unstable in our previous work on type A

459 defect, spontaneously shifting toward the A1. For this reason, we do not have any evidence of the
460 signal reported by Fleet et al. (2011).

461 Despite these small deviations, there is a general good agreement with the experimental results,
462 especially with those of synthetic carbonated hydroxylapatite samples (Fathi et al., 2008; Fleet and
463 Liu, 2007; Sturgeon and Brown, 2009). Both natural and synthetic samples present different
464 concentration of type A and type B defects and their distribution within the lattice is not clearly
465 known. An important aspect may be given by the presence and the content in the apatite cell of
466 various type of defects, substituent and/or vacancies, especially for bone tissues samples. When
467 modeling a structure different strategies have been proposed to restore the neutrality of the apatite
468 cell when a type B carbonate ion is included (Astala and Stott, 2005; Peroos et al., 2006). We have
469 chosen the $Ca^{2+} \rightarrow Na^{+}$ substitution because the sodium ion was observed in biological apatites and
470 its ionic radius is very close to that of calcium ion. This approach affected the COHAp lattice and
471 phonon modes as we reported, while other possible ways were not covered in the present work. As
472 an example, the inclusion of an OH group in the cell near the carbonate ion may produce different
473 responses. However, that simulation will be the subject of a future work.

474

475 **References cited**

476 Astala, R., and Stott, M.J. (2005) First principles investigation of mineral component of bone: CO3
477 substitutions in hydroxyapatite. Chemistry of Materials, 17(16), 4125-4133.
478 Becke, A.D. (1993) A New Mixing of Hartree-Fock and Local Density-Functional Theories. Journal of
479 Chemical Physics, 98(2), 1372-1377.
480 Catti, M., Pavese, A., Dovesi, R., and Saunders, V.R. (1993) Static lattice and electron properties of MgCO3
481 (Magnesite) calculated by ab-initio periodic Hartree-Fock methods. Phys. Rev. B, 47, 9189-9198.
482 Cora, F., Alfredsson, M., Mallia, G., Middlemiss, D.S., Mackrodt, W.C., Dovesi, R., and Orlando, R. (2004)
483 The performance of hybrid density functionals in solid state chemistry. In N.M.J.E. Kaltsoyannis,
484 Ed. Principles and Applications of Density in Inorganic Chemistry Ii, 113, p. 171-232.
485 Corno, M., Busco, C., Civalleri, B., and Ugliengo, P. (2006) Periodic ab initio study of structural and
486 vibrational features of hexagonal hydroxyapatite Ca10(PO4)6(OH)2. Phys. Chem. Chem. Phys., 8,
487 2464-2472.
488 Dorozhkin, S.V. (2009a) Calcium orthophosphate-based biocomposites and hybrid biomaterials. Journal of
489 Materials Science, 44(9), 2343-2387.
490 -. (2009b) Calcium Orthophosphate Cements and Concretes. Materials, 2, 221-291.
491 -. (2009c) Calcium Orthophosphates in Nature, Biology and Medicine. Materials, 2, 399-398.
492 -. (2009d) Nanodimensional and Nanocrystalline Apatites and Other Calcium Orthophosphates in
493 Biomedical Engineering, Biology and Medicine. Materials, 2, 1975-2045.

Dovesi, R., Roetti, C., Freyria Fava, C., Prencipe, M., and Saunders, V.R. (1991) On the elastic properties of lithium, sodium an potassium oxide. An ab initio study. Chemical Physics, 156, 11-19.

Dovesi, R., Saunders, V.R., Roetti, C., Orlando, R., Zicovich-Wilson, C.M., Pascale, F., Civalleri, B., Doll, K., Harrison, N.M., Bush, I.J., D'Arco, P., and Llunell, M. (2009) CRYSTAL09 User's Manual. University of Torino, Torino.

Engin, A., and Girgin, I. (2009) Synthesis of hydroxyapatite by using calcium carbonate and phosphoric acid in various water-ethanol solvent systems. Central European Journal of Chemistry, 7(4), 745-751.

Fathi, M.H., Hanifi, A., and Mortazavi, V. (2008) Peparation and bioactivity evaluation of bone-like hydroxyapatite nanopowder. J. Mater. Process. Tech., 202, 536-542.

Fleet, M.E. (2009) Infrared spectra of carbonate apatites: n2-Region bands. Biomaterials, 30, 1473-1481.

Fleet, M.E., and Liu, X. (2007) Coupled substitution of type A and B carbonate in sodium-bearing apatite. Biomaterials, 28(6), 916-926.

-. (2008) Type A-B carbonate chlorapatite synthesized at high pressure. Journal of Solid State Chemistry, 181(9), 2494-2500.

Fleet, M.E., and Liu, X.Y. (2003) Carbonate apatite type A synthesized at high pressure: new space group (P(3)over-bar) and orientation of channel carbonate ion. Journal of Solid State Chemistry, 174(2), 412-417.

-. (2004) Location of type B carbonate ion in type A-B carbonate apatite synthesized at high pressure. Journal of Solid State Chemistry, 177(9), 3174-3182.

-. (2005) Local structure of channel ions in carbonate apatite. Biomaterials, 26(36), 7548-7554.

Fleet, M.E., Liu, X.Y., and King, P.L. (2004) Accommodation of the carbonate ion in apatite: An FTIR and X-ray structure study of crystals synthesized at 2-4 GPa. American Mineralogist, 89(10), 1422-1432.

Fleet, M.E., Liu, X.Y., and Liu, X. (2011) Orientation of channel carbonate ions in apatite: Effect of pressure and composition. American Mineralogist, 96(7), 1148-1157.

Gibson, I.R., and Bonfield, W. (2002) Novel synthesis and characterization of an AB-type carbonate-substituted hydroxyapatite. Journal of Biomedical Materials Research, 59(4), 697-708.

Kovaleva, E.S., Shabanov, M.P., Putlyaev, V.I., Tretyakov, Y.D., Ivanov, V.K., and Silkin, N.I. (2009) Bioresorbable carbonated hydroxyapatite $Ca_{10-x}Na_x(PO_4)_{6-x}(CO_3)_x(OH)_2$ powders for bioactive materials preparation. Cent. Eur. J. Chem, 7(2), 168-174.

Lafon, J.P., Champion, E., and Bernache-Assollant, D. (2008) Processing of AB-type carbonated hydroxyapatite Ca10-x(PO4)(6-x)(CO3)(x)(OH)(2-x-2y)(CO3)(y) ceramics with controlled composition. Journal of the European Ceramic Society, 28(1), 139-147.

Lee, C.T., Yang, W.T., and Parr, R.G. (1988) Development of the Colle-Salvetti Correlation-Energy Formula into a Functional of the Electron-Density. Physical Review B, 37(2), 785-789.

LeGeros, R.Z. (2002) Properties of osteoconductive biomaterials: Calcium phosphates. Clinical Orthopaedics and Related Research(395), 81-98.

Lindberg, B. (1988) A New Efficient Method for Calculation of Energy Eigenvalues and Eigenstates of the One-Dimensional Schrodinger-Equation. Journal of Chemical Physics, 88(6), 3805-3810.

Momma, K., and Izumi, F. (2008) VESTA: a three-dimensional visualization system for electronic and structural analysis. J. Appl. Crystallogr., 41, 653-658.

Monkhorst, H.J., and Pack, J.D. (1976) Phys. Rev. B, 8, 5188-5192.

Pascale, F., Zicovich-Wilson, C.M., Gejo, F.L., Civalleri, B., Orlando, R., and Dovesi, R. (2004) The calculation of the vibrational frequencies of crystalline compounds and its implementation in the CRYSTAL code. Journal of Computational Chemistry, 25(6), 888-897.

Pascale, F., Zicovich-Wilson, C.M., Orlando, R., Roetti, C., Ugliengo, P., and Dovesi, R. (2005) Vibration frequencies of $Mg_3Al_2Si_3O_{12}$ pyrope. An ab initio study with the CRYSTAL code. Journal of Physical Chemistry B, 109(13), 6146-6152.

Peeters, A., DeMaeyer, E.A.P., VanAlsenoy, C., and Verbeeck, R.M.H. (1997) Solids modeled by ab initio crystal-field methods .12. Structure, orientation, and position of A-type carbonate in a hydroxyapatite lattice. Journal of Physical Chemistry B, 101(20), 3995-3998.

Penel, G., Delfosse, C., Descamps, M., and Leroy, G. (2005) Composition of bone and apatitic biomaterials as revealed by intravital Raman microspectroscopy. Bone.

Peroos, S., Du, Z., and de Leeuw, N.H. (2006) A computer modelling study of the uptake, structure and distribution of carbonate defects in hydroxy-apatite. Biomaterials, 27, 2150-2161.

Petra, M., Anastassopopulou, J., Theologis, T., and Theophanides, T. (2005) Synchrotron mirco-FT-IR spectroscopic evaluation of normal paediatric human bone. J Mol Struct, 733, 101-110.

Prencipe, M., Pascale, F., Zicovich-Wilson, C.M., Saunders, V.R., Orlando, R., and Dovesi, R. (2004) The vibrational spectrum of calcite (CaCO3): an ab initio quantum-mechanical calculation. Physics and Chemistry of Minerals, 31(8), 559-564.

Rabone, J.A.L., and de Leeuw, N.H. (2007) Potential routes to carbon inclusion in apatite materials: a DFT study. Phys. Chem. Miner., 34, 495-506.

Rehman, I., and Bonfield, W. (1997) Characterization of hydroxyapatite and carbonated apatite by photo acoustic FTIR spectroscopy. Journal of Materials Science-Materials in Medicine, 8(1), 1-4.

Sturgeon, J.L., and Brown, P.W. (2009) Effects of carbonate on hydroxyapatite formed from $CaHPO_4$ and $Ca_4(PO_4)_2O$. Journal of Materials Science: Materials in Medicine, 20, 1787-1794.

Suda, H., Yashima, M., Kakihana, M., and Yoshimura, M. (1995) Monoclinic <--> Hexagonal Phase Transition in Hydroxyapatite Studied by X-ray Powder Diffraction and Differential Scanning Calorimeter Techniques. Journal of Physical Chemistry, 99(17), 6752-6754.

Suetsugu, Y., Shimoya, I., and Tanaka, J. (1998) Configuration of Carbonate Ions in Apatite Structure Determined by Polarized Infrared Spectroscopy. J. Am. Ceram. Soc., 81, 746-748.

Tosoni, S., Pascale, F., Ugliengo, P., Orlando, R., Saunders, V.R., and Dovesi, R. (2005) Quantum mechanical calculation of the OH vibrational frequency in crystalline solids. Molecular Physics, 103(18), 2549-2558.

Tsuda, H., and Arends, J. (1994) Orientational micro-Raman spectroscopy on hydroxyapatite single crystals and human enamel crystallites. Journal of Dental Research, 73, 1703-1710.

Ugliengo, P., Pascale, F., Merawa, M., Labeguerie, P., Tosoni, S., and Dovesi, R. (2004) Infrared spectra of hydrogen-bonded ionic crystals: Ab initio study of Mg(OH)(2) and beta-Be(OH)(2). Journal of Physical Chemistry B, 108(36), 13632-13637.

Ugliengo, P., Viterbo, D., and Chiari, G. (1993) MOLDRAW: molecular graphic on a personal computer. Zeitschrift Fur Kristallographie, 207, 9-23.

Ulian, G., Valdrè, G., Corno, M., and Ugliengo, P. (2013a) Periodic ab initio bulk investigation of hydroxylapatite and type A carbonated apatite with both pseudopotential and all electron basis sets for calcium atoms. American Mineralogist, 98(2-3), 410-416.

-. (2013b) The vibrational features of hydroxylapatite and type A carbonated apatite: a first principle contribution. American Mineralogist, Accepted, in press 2013.

Valenzano, L., Torres, F.J., Klaus, D., Pascale, F., Zicovich-Wilson, C.M., and Dovesi, R. (2006) Ab initio study of the vibrational spectrum and related properties of crystalline compounds; the case of CaCO3 calcite. Zeitschrift Fur Physikalische Chemie-International Journal of Research in Physical Chemistry & Chemical Physics, 220(7), 893-912.

Yahia, F.B.H., and Jemal, M. (2010) Synthesis, structural analysis and thermochemistry of B-type carbonate apatites. Thermochimica Acta, 505(1-2), 22-32.

588 **LIST OF TABLES**
589

Table 1. Optimization results for the type B COHAp substitution.

	OHAp*	**Na position**									
		1	**2**	**3**	**4**	**5**	**6**	**7**	**8**	**9**	**10**
Cell parameters											
a (Å)	9.433	9.377	*9.432*	9.376	9.398	9.402	*9.413*	9.373	9.397	9.429	9.386
b (Å)	9.433	9.346	*9.335*	9.335	9.310	9.364	*9.301*	9.320	9.353	9.338	9.324
c (Å)	6.896	6.924	*6.898*	6.910	6.899	6.913	*6.889*	6.926	6.915	6.895	6.903
α (°)	90	90.8	*90.4*	90.6	90.0	90.1	*90.1*	90.6	90.2	90.4	90.2
β (°)	90	90.0	*89.2*	90.3	90.0	90.3	*90.1*	90.2	90.1	89.7	90.2
γ (°)	120	120.6	*120.8*	120.3	120.5	121.0	*120.0*	120.8	121.1	120.8	120.3
Volume ($Å^3$)	531.5	522.3	*521.8*	521.9	520.1	521.6	*522.2*	519.5	520.7	521.2	521.4
Density (g/cm^3)	3.139	3.025	*3.028*	3.027	3.038	3.029	*3.025*	3.041	3.034	3.031	3.03
Mean bond lengths (Å)											
P - O	1.552	1.551	*1.552*	1.552	1.552	1.551	*1.551*	1.552	1.551	1.551	1.551
O - H	0.972	0.970	*0.971*	0.970	0.970	0.973	*0.971*	0.972	0.972	0.970	0.969
O-H --- O-H	2.477	2.232	*2.125*	2.406	2.110	2.036	*2.386*	1.994	2.058	2.312	2.666
C - O	-	1.295	*1.293*	1.294	1.295	1.294	*1.293*	1.294	1.294	1.294	1.295
Ca --- O	2.437	2.423	*2.445*	2.426	2.448	2.445	*2.446*	2.450	2.448	2.447	2.433
Na --- O	-	2.646	*2.555*	2.522	2.505	2.557	*2.477*	2.430	2.480	2.513	2.486
Na (--- $O_{PO4exited}$)	-	4.939	*2.762*	4.754	3.957	4.478	*2.342*	2.501	3.456	4.7844	5.346
Ca3 --- Ca3	4.178	4.073	*4.086*	4.069	4.090	4.084	*4.062*	4.064	4.070	4.073	4.088
Na --- C	-	3.354	*3.616*	3.326	3.423	3.146	*3.285*	3.373	3.456	5.800	6.177
Na --- O(CO3)	-	2.686	*2.775*	2.825	2.358	2.347	*2.589*	2.594	2.791	4.892	5.724
(Na--C)/(Na--O)	-	1.25	*1.30*	1.18	1.45	1.34	*1.27*	1.30	1.24	1.19	1.08
Mean bond angles (°)											
O - P -O	109.8	109.2	*109.3*	109.3	109.3	109.8	*110.0*	109.6	109.5	109.5	109.4
O - C -O	-	120.0	*120.0*	120.0	120.0	120.0	*120.0*	120.0	120.0	120.0	120.0
ΔE (kJ/mol)	-	9.3	*1.5*	18.4	18.2	28.8	*0.00*	13.9	39.3	46.3	50.2
Band Gap (eV)	7.71	7.76	*7.84*	7.64	7.79	7.96	*7.66*	7.93	7.87	7.60	7.76

Notes: values in italic indicate the most stable structures obtained. Numbers from 1 to 10 indicate the location of Na^+/Ca^{2+} substitution.
* (Ulian et al., 2013a)

590
591

592

Table 2. Optimization results for type A-B CAp in comparison with experimental data

Defect A-B (Na)	**Experimental***	**B3LYP**	
Single Cell	**XRD**	**Na2**	**Na6**
Cell parameters			
a (Å)	9.3855	9.4085(+0.023)	9.3951(+0.010)
b (Å)	9.3855	9.4111(+0.026)	9.3371(-0.048)
c (Å)	6.9142	6.9210(+0.007)	6.9038(-0.010)
α (°)	90.0	89.0(-1.0)	89.6(-0.4)
β (°)	90.0	90.9(+0.9)	90.4(+0.4)
γ (°)	120.0	120.1(+0.1)	119.8(-0.2)
Volume ($Å^3$)	527.5	530.1(+2.6)	525.8(-1.7)
Density (g/cm^3)	3.120	3.066(-0.054)	3.091(-0.029)
% CO_3 wt.	11.1	12.3(+1.2)	12.3(+1.2)
% Na wt.	2.01	2.35(+0.34)	2.35(+0.34)
Mean bond lengths			
P – O	1.513	1.544(+0.031)	1.552(+0.039)
C - O (A)	-	1.294	1.295
C - O (B)	-	1.295	1.296
C – C	-	3.854	3.881
Ca --- O (A)	2.360	2.378(+0.018)	2.422(+0.062)
Na --- O	-	2.568	2.395
Ca3 --- Ca3	4.212	4.306(+0.094)	4.257(+0.045)
Na --- C (A)	-	5.138	2.818
Na --- C (B)	-	3.649	3.187
Na --- O(CO_3)	-	2.732	2.287
(Na--C)/(Na--O)	-	1.336	1.394
Mean bond angles			
O - P –O	109.4	110.1(+0.7)	110.0(+0.6)
O - C -O (A)	120.0	120.0(+0.0)	120.0(+0.0)
O - C -O (B)	120.0	120.0(+0.0)	120.0(+0.0)
Energy			
ΔE (kJ/mol)	-	+19.06	0.00

Notes: values in parenthesis are the deviations from experimental results. Na2 and Na6 indicate the location of Na^+/Ca^{2+} substitution.
* (Fleet and Liu, 2007)

593
594

595

Table 3. Optimization results for type A-B COHAp

Defect A-B (Na)	**Experimental***	**B3LYP**		
2 x 2 x 1 unit-cell	**XRD**	**AB-1**	**AB-2**	**AB-3**
Cell parameters				
a (Å)	9.397	9.451(+0.054)	9.413(+0.016)	9.486(+0.089)
b (Å)	9.397	9.482(+0.085)	9.466(+0.069)	9.400(+0.003)
c (Å)	6.889	6.897(+0.008)	6.903(+0.014)	6.906(+0.017)
α (°)	90.0	89.5(-0.5)	89.5(-0.5)	89.9(-0.1)
β (°)	90.0	90.1(+0.1)	90.4(+0.4)	90.0(+0.0)
γ (°)	120.0	120.6(+0.6)	120.1(+0.1)	120.1(+0.1)
Volume ($Å^3$)	526.8	532.0(+5.2)	532.2(+5.4)	532.5(+5.7)
Density (g/cm^3)	3.150	3.112(-0.038)	3.111(-0.039)	3.109(-0.041)
% CO_3 wt.	3.5	3.01(-0.49)	3.01(-0.49)	3.01(-0.49)
% Na wt.	0.81	0.58(-0.23)	0.58(-0.23)	0.58(-0.23)
Mean bond lengths				
P - O	-	1.548	1.548	1.548
O - H	-	0.972	0.971	0.971
O-H --- O-H	-	2.537	2.491	2.440
C - O (A)	-	1.287	1.287	1.288
C - O (B)	-	1.294	1.295	1.296
C - C	-	8.108	8.693	5.988
Ca --- O (A)	-	2.415	2.339	2.371
Na --- O	-	2.403	2.421	2.407
Ca3 --- Ca3	-	4.237	4.343	4.239
Na --- C (A)	-	8.591	9.921	7.363
Na --- C (B)	-	3.122	3.330	3.104
Na --- O(CO3)	-	2.322	2.484	2.483
(Na--C)/(Na--O)	-	1.345	1.341	1.250
Mean bond angles				
O - P -O	-	109.4	108.9	108.9
O - C -O (A)	-	120.0	120.0	120.0
O - C -O (B)	-	120.0	120.0	120.0
Energy				
ΔE (kJ/mol)	-	0.00	20.71	9.18

Notes: values in parenthesis are the deviations from experimental results.
* Single-crystal XRD refinement of sample LM006, (Fleet and Liu, 2007)

596
597
598
599
600
601
602
603
604
605
606
607
608

609
610

Table 4. Comparison between C(OH)Ap models and natural hard tissues

	Theoretical models					Experimental§		
	OHAp*	**Type A1 CAp***	**Type B Na-COHAp†**	**Type A-B Na-CAp†**	**Type A-B Na-COHAp†**	**Bone**	**Dentin**	**Enamel**
Cell parameters								
a (Å)	9.433	9.582	9.3982	9.4027	*9.4493*	9.41	9.421	*9.441*
b (Å)	9.433	9.764	9.3327	9.3707	*9.4486*	9.41	9.421	*9.441*
c (Å)	6.896	6.877	6.9071	6.9134	*6.9028*	6.89	6.887	*6.880*
α (°)	90	89.3	90.3	89.3	*89.6*	90.0	90.0	*90*
β (°)	90	89.8	90.0	90.7	*90.2*	90.0	90.0	*90*
γ (°)	120	121.9	120.6	120.0	*120.3*	120.0	120.0	*120*
Volume (Å^3)	531.5	546	521.3	527.4	*532.2*	528.4	529.4	*531.1*
% wt.								
Ca^{2+}	39.89	38.81	37.87	36.79	*39.07*	34.80	35.1	*36.5*
P	18.05	18.05	16.26	15.84	*17.86*	15.20	16.9	*17.7*
CO_3^{2-}	-	5.82	6.30	12.26	*3.01*	7.40	5.6	*3.5*
Na^+	-	-	2.41	2.35	*0.58*	0.90	0.6	*0.5*

* (Ulian et al., 2013a)
† present work
§ (Dorozhkin, 2009c)

611
612
613

Table 5. Carbonate ion phonon frequencies in type B COHAp

Band	**Na1**	**Na2**	**Na3**	**Na4**	**Na5**	**Na6**	**Na7**	**Na8**	**Na9**	**Na10**
$\nu_4(CO_3)$	-4	-1	-8	-4	-8	706	-12	-13	-5	-7
$\nu_4(CO_3)$	-3	-3	-6	-8	-2	715	9	2	-4	-8
$\nu_2(CO_3)$	0	-1	5	5	3	876	-1	3	3	4
$\nu_1(CO_3)$	-9	1	-3	-16	-5	1109	-3	-4	-3	-10
$\nu_3(CO_3)$	-25	6	-5	-23	8	1481	-1	-16	20	6
$\nu_{3b}(CO_3)$	-1	-16	-31	-8	-40	1562	-20	-11	-48	-53

Notes: Values (cm^{-1}) are reported as deviation from the most stable type B COHAp structure (Na6).

614
615
616
617
618
619
620
621
622
623
624
625
626
627
628
629
630
631

Table 6. Carbonate ion phonon frequencies in different type A-B models

Band	AB-Na6	AB-1	AB-2	AB-3	B-Na6
$\nu_{4a}(CO_3)$ (A)	660	666	676	666	-
$\nu_{4b}(CO_3)$ (A)	759	784	775	771	-
$\nu_2(CO_3)$ (A)	890	889	882	889	-
$\nu_1(CO_3)$ (A)	1086	1128	1124	1125	-
$\nu_3(CO_3)$ (A)	1442	1503	1517	1501	-
$\nu_{3b}(CO_3)$ (A)	1589	1612	1608	1613	-
$\nu_{4a}(CO_3)$ (B)	693	693	692	701	706
$\nu_{4b}(CO_3)$ (B)	721	719	713	718	715
$\nu_2(CO_3)$ (B)	875	879	879	861	876
$\nu_1(CO_3)$ (B)	1091	1099	1095	1092	1109
$\nu_{3a}(CO_3)$ (B)	1463	1472	1473	1462	1481
$\nu_{3b}(CO_3)$ (B)	1545	1568	1548	1553	1562

Notes: Values are in wavenumber (cm^{-1}).

Table 7. Comparison between theoretical and experimental phonon results for C(OH)Ap structures.

Band	Theoretical				Experimental				
	A1[a]	*B-Na6*[b]	*AB-Na6*[b]	*AB-1*[b]	*Raman*[c]	*Micro-FTIR*[d]	*FTIR*[e]	*FTIR*[f]	*FTIR*[g]
$\nu_{4a}(CO_3)$ (A)	670	-	660	666	676	670	-	-	-
$\nu_{4b}(CO_3)$ (A)	781	-	759	784	754	750	-	-	-
$\nu_2(CO_3)$ (A)	878	-	890	889	-	878	-	880	-
$\nu_1(CO_3)$ (A)	1134	-	1086	1128	1103	-	-	-	-
$\nu_3(CO_3)$ (A)	1518	-	1442	1503	-	-	1449	1457	-
$\nu_{3b}(CO_3)$ (A)	1604	-	1589	1612	-	-	1541	1550	1558
$\nu_{4a}(CO_3)$ (B)	-	706	693	693	689	670	-	-	
$\nu_{4b}(CO_3)$ (B)	-	715	721	719	718	750	-	-	
$\nu_2(CO_3)$ (B)	-	876	875	879	-	871	873	876	873
$\nu_1(CO_3)$ (B)	-	1109	1091	1099	1073	-	-	-	-
$\nu_{3a}(CO_3)$ (B)	-	1481	1463	1472	-	-	1406	1418	1423
$\nu_{3b}(CO_3)$ (B)	-	1562	1545	1568	-	-	1474	1462	1473

Notes: all values are in wavenumbers (cm^{-1}).
a (Ulian et al., 2013b)
b present work
c (Penel et al., 2005)
d (Petra et al., 2005)
e (Fleet and Liu, 2008)
f (Fathi et al., 2008)
g (Sturgeon and Brown, 2009)

LIST OF FIGURES

Figure 1. Views along the [001] direction of OHAp unit cell content with labelled potential substitution sites.

Figure 2. Optimization results for the two most stable type B COHAp, with (a) Na2/Ca2 and (b) Na6/Ca6 substitutions. Atoms are indicated in red for oxygen, pink for phosphate, cyan for calcium, white for hydrogen, ochre for carbon and yellow for sodium.

Figure 3. Views along (a,b) [001] and (c,d) [110] directions of the unit-cell phosphate ion in OHAp (a,c) interested in the type B CO_3^{2-} substitution (b,d). The sloping face in which the carbonate ion was introduced is maintained in the type B COHAp to show the optimization effect.

Figure 4. Substitution scheme for type A-B COHAp. (a) Generation of the supercell and (b) generation of the three type A-B models. A and B refers to the carbonate defect types and OH to the pure hydroxylapatite.

Figure 5. Simulated vibrational spectra of the most stable type B COHAp structure (Na6 model).

Figure 6. Simulated ν_3 and ν_2 bands of carbonate ion in the type B COHAp models. Dotted lines are centered on the Na6 model results.

Figure 7. Phonon spectra of mixed type A-B C(OH)Ap structures (a) in single unit-cell and (b) in 2x2x1 supercell. The dotted line in (a) is the same type A-B CAp spectrum, with sharper signals. For the sake of clearness, in the spectra reported in (b) the A1 and B modes have been labeled as (*) and (°), respectively.

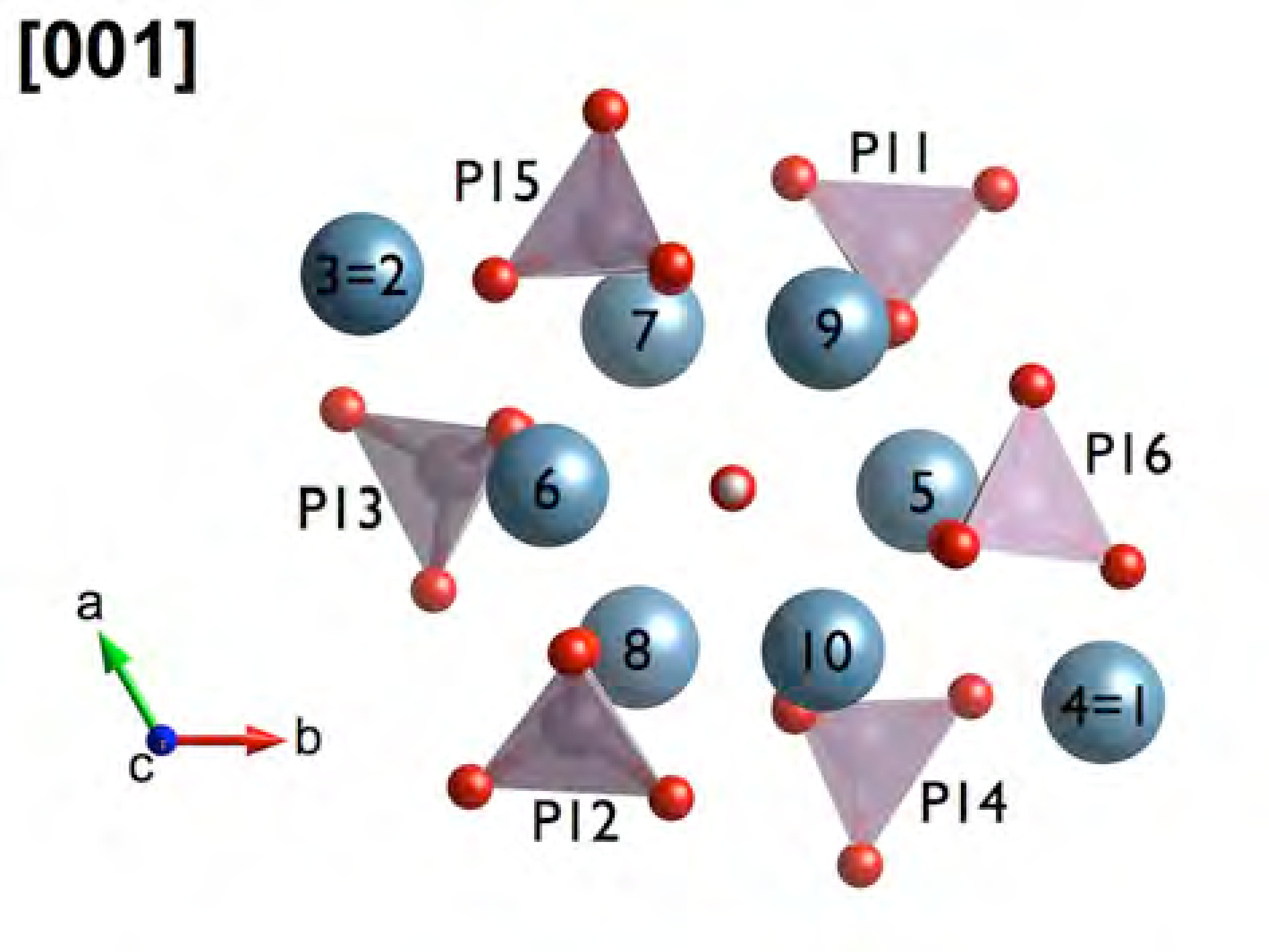
[001]
PI5
PI1
3=2
7
9
PI3
6
5
PI6
a
b
c
8
10
4=1
PI2
PI4

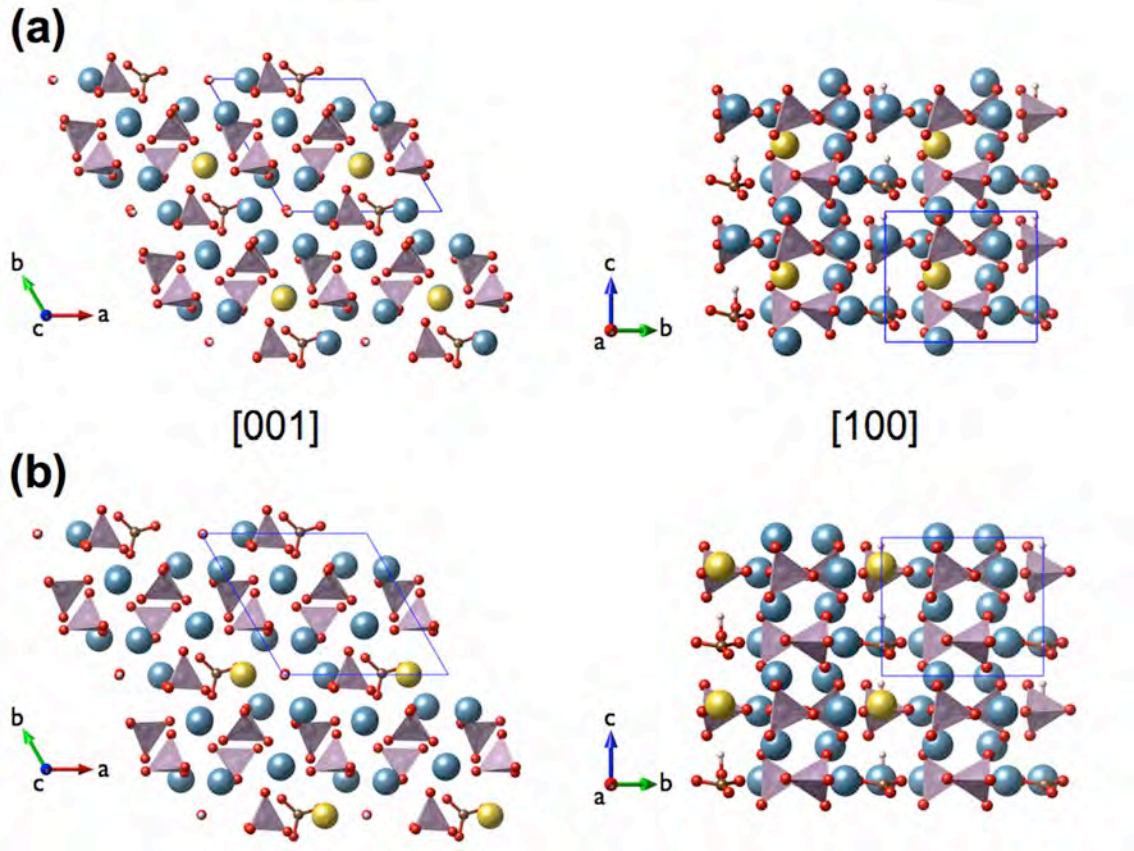
(a)
b
c
a
c
a
b
[001]
[100]
(b)
b
c
a
c
a
b

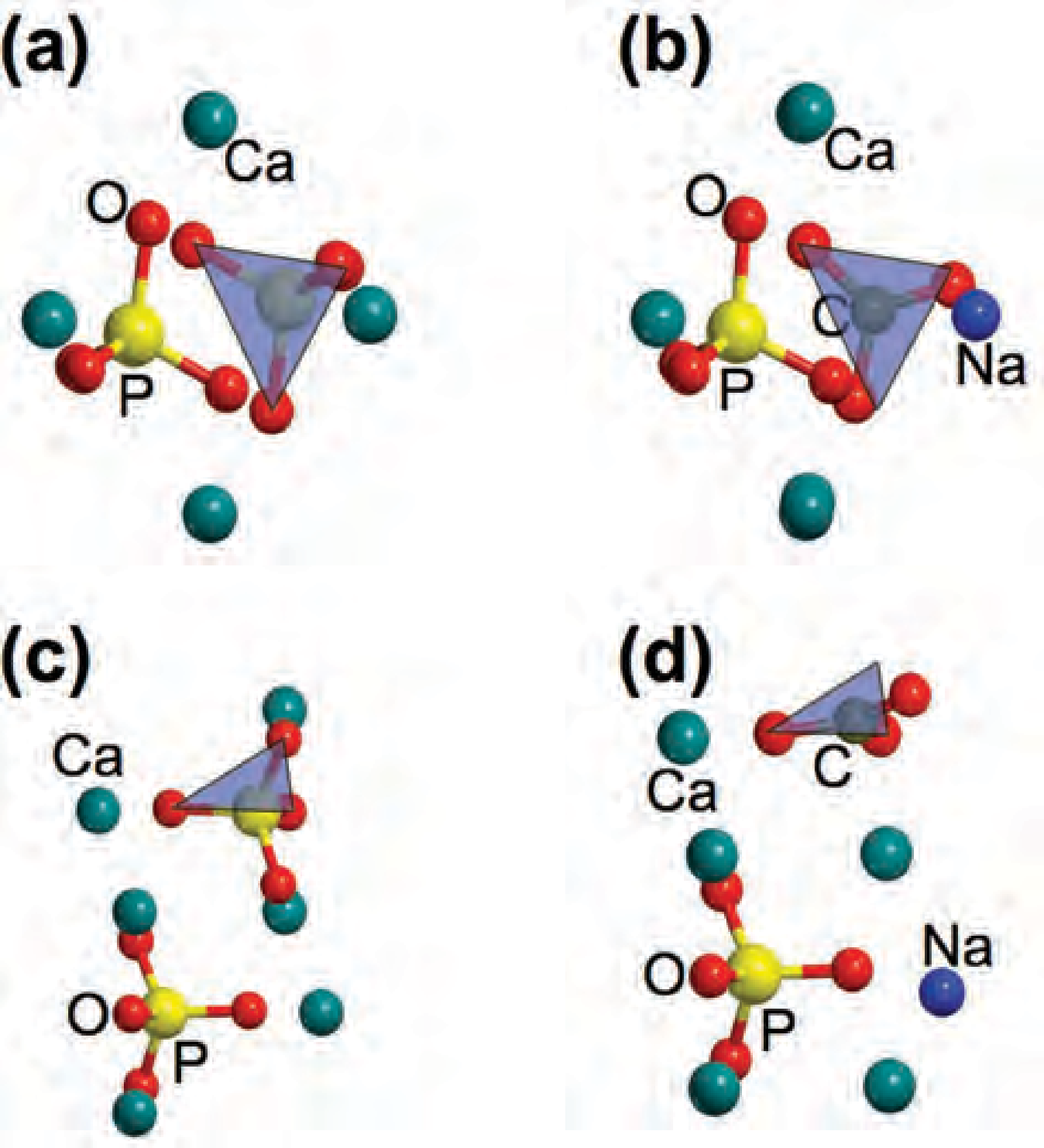
(a)
Ca
O
P
(b)
Ca
O
C
Na
P
(c)
Ca
O
P
(d)
C
Ca
Na
O
P

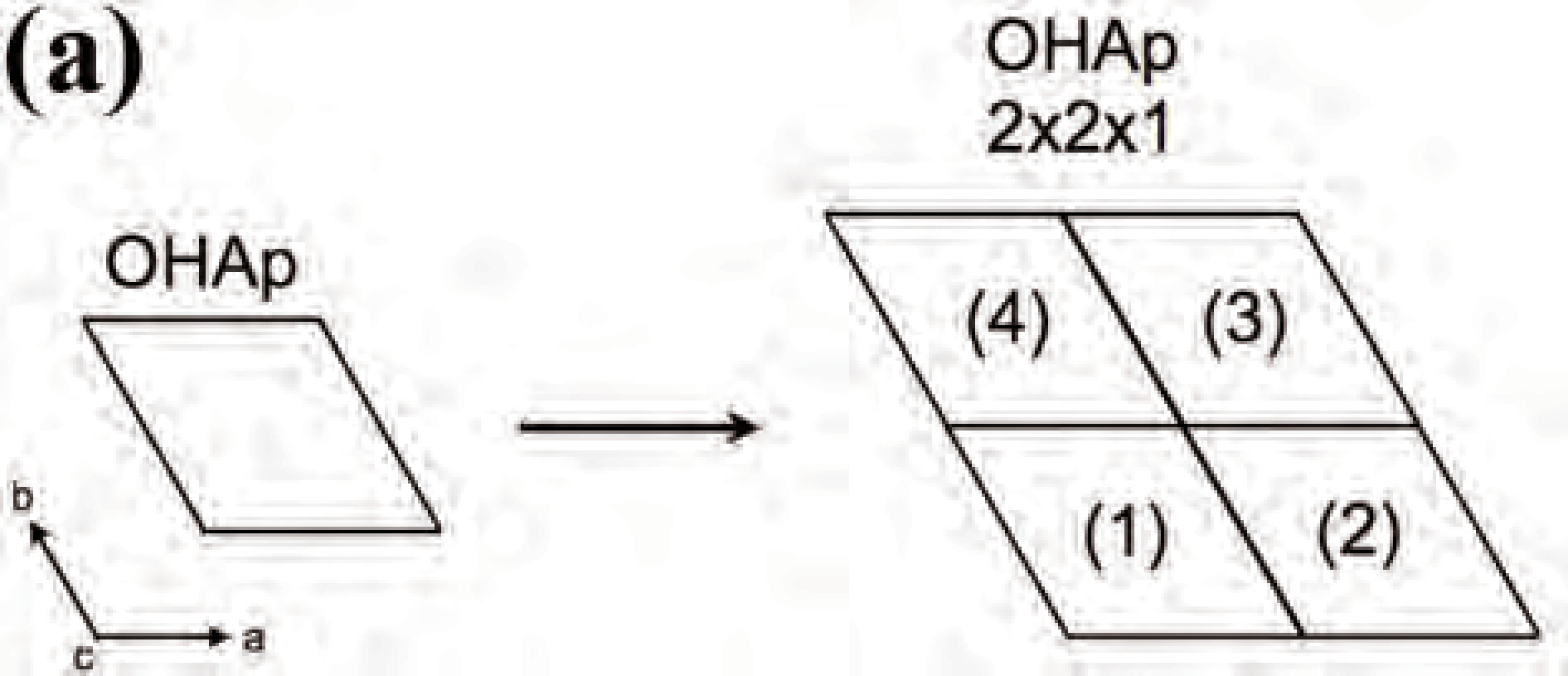
(a)
OHAp
OHAp
2x2x1
(4)
(3)
(1)
(2)
b
c
a

(b)

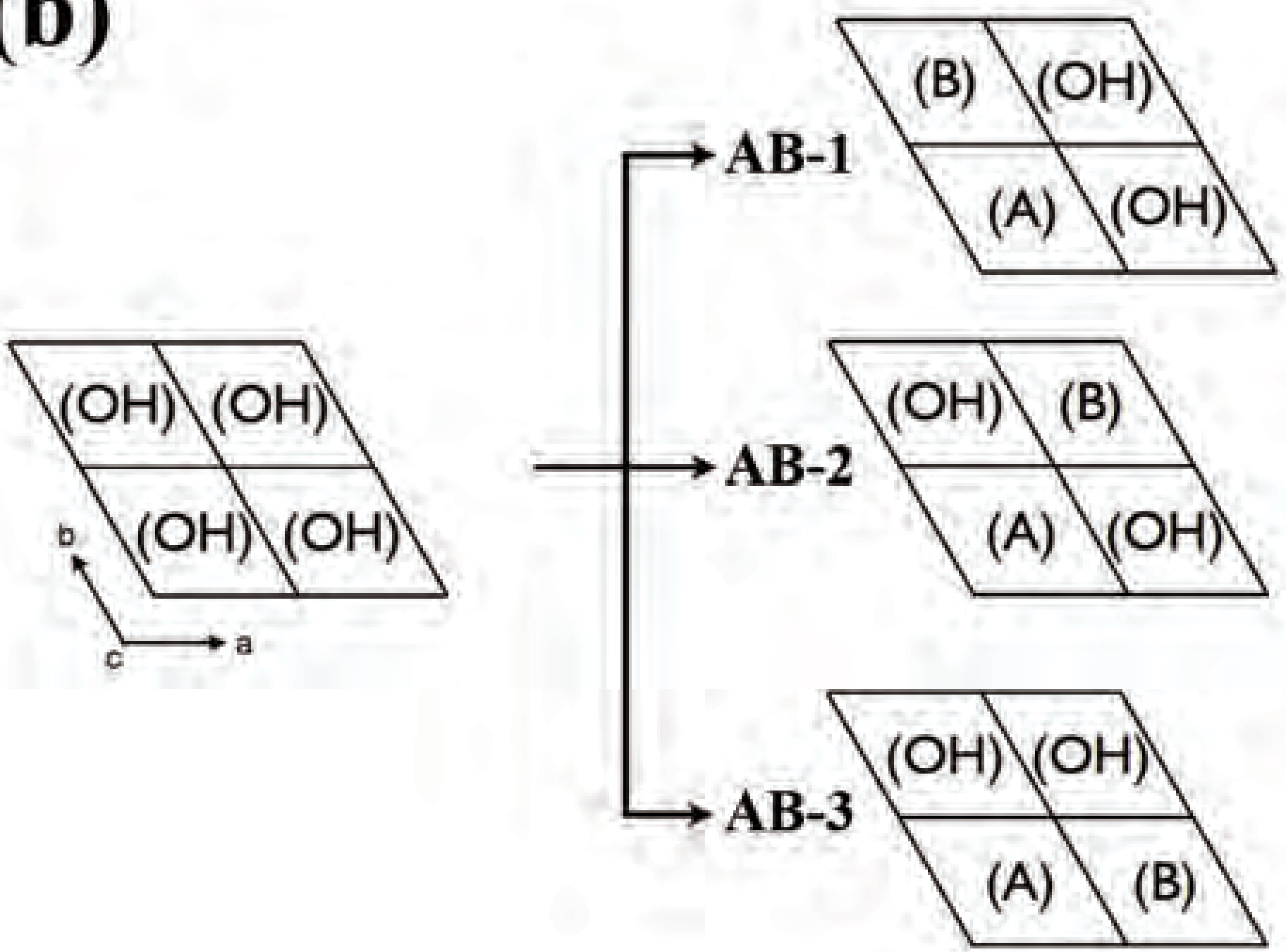

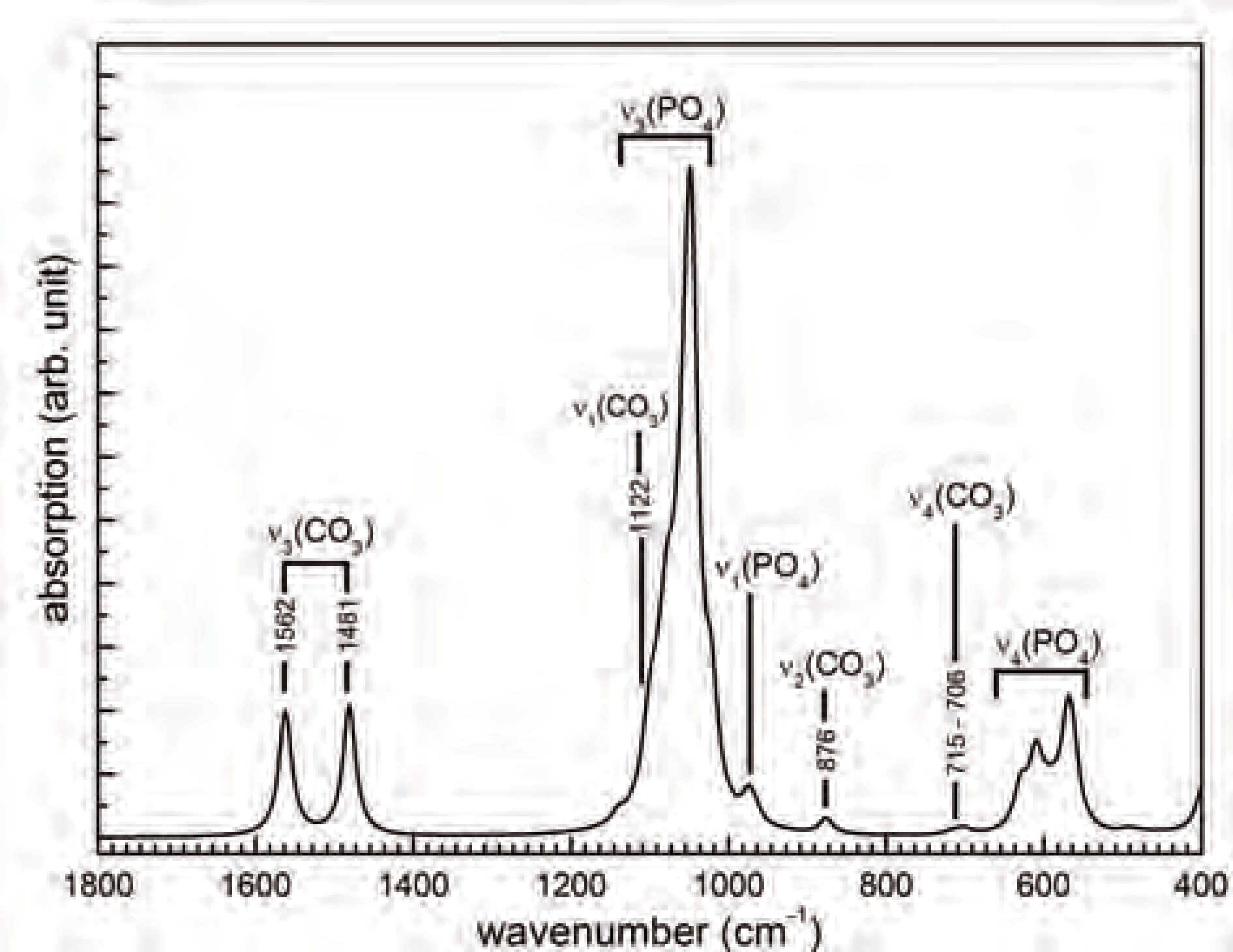
absorption (arb. unit)
$\nu_3(PO_4)$
$\nu_1(CO_3)$
1122
$\nu_3(CO_3)$
1562
1461
$\nu_1(PO_4)$
$\nu_2(CO_3)$
876
$\nu_4(CO_3)$
715 - 706
$\nu_4(PO_4)$
1800
1600
1400
1200
1000
800
600
400
wavenumber (cm^{-1})

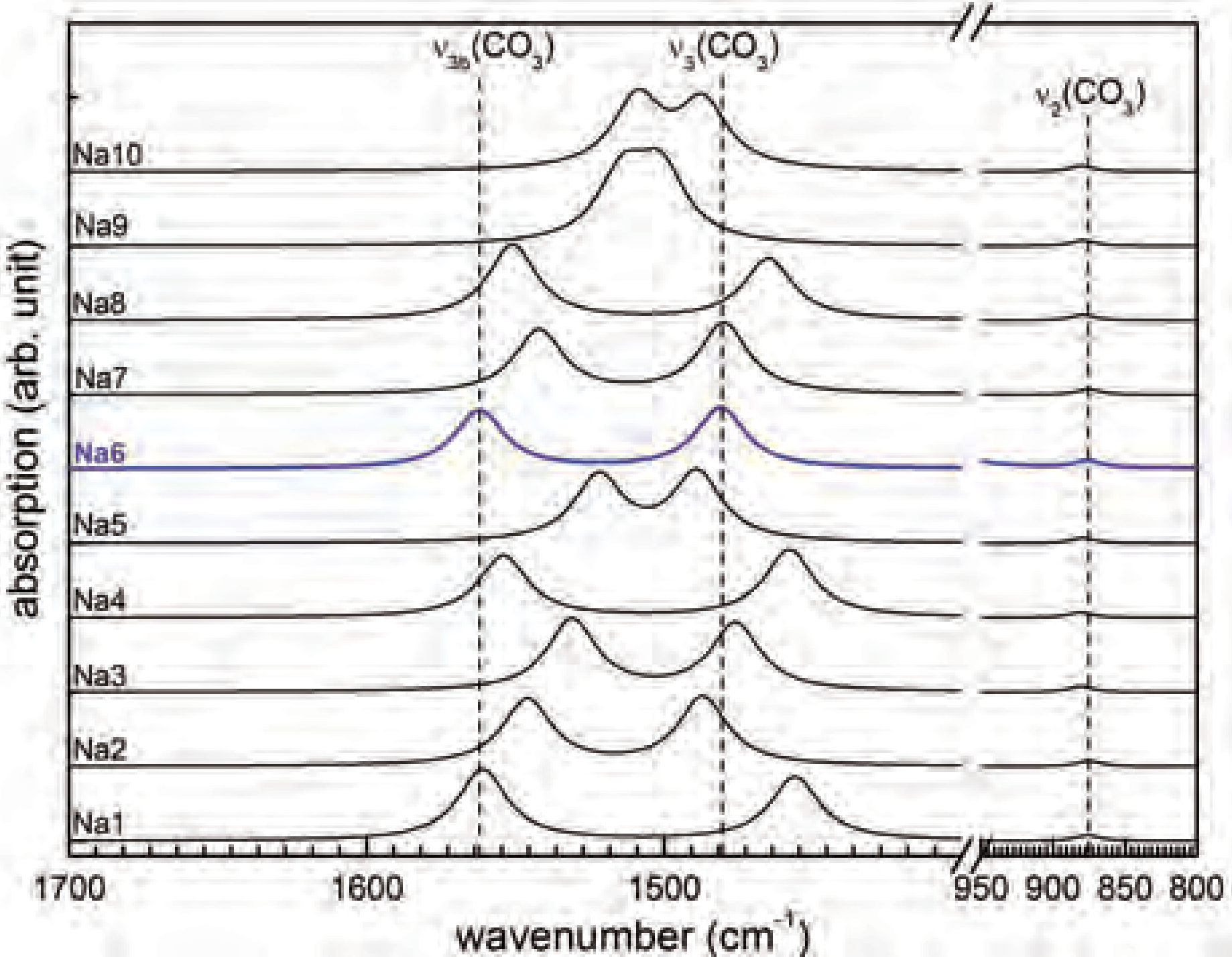
$\nu_{3b}(CO_3)$
$\nu_3(CO_3)$
$\nu_2(CO_3)$
Na10
Na9
Na8
Na7
Na6
Na5
Na4
Na3
Na2
Na1
absorption (arb. unit)
1700
1600
1500
950
900
850
800
wavenumber (cm^{-1})

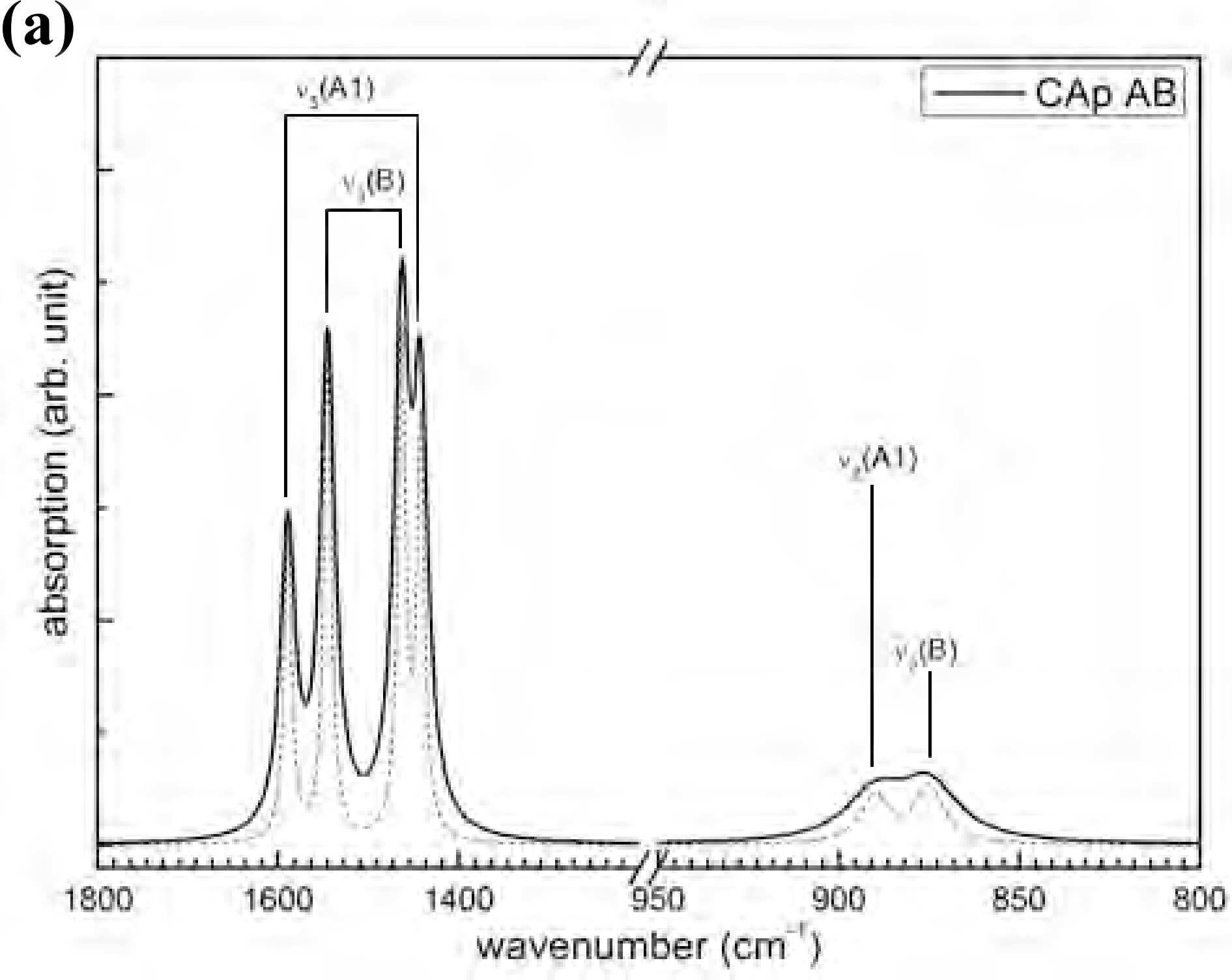
(a)
CAp AB
ν_3(A1)
ν_1(B)
ν_2(A1)
ν_4(B)
absorption (arb. unit)
1800
1600
1400
950
900
850
800
wavenumber (cm^{-1})

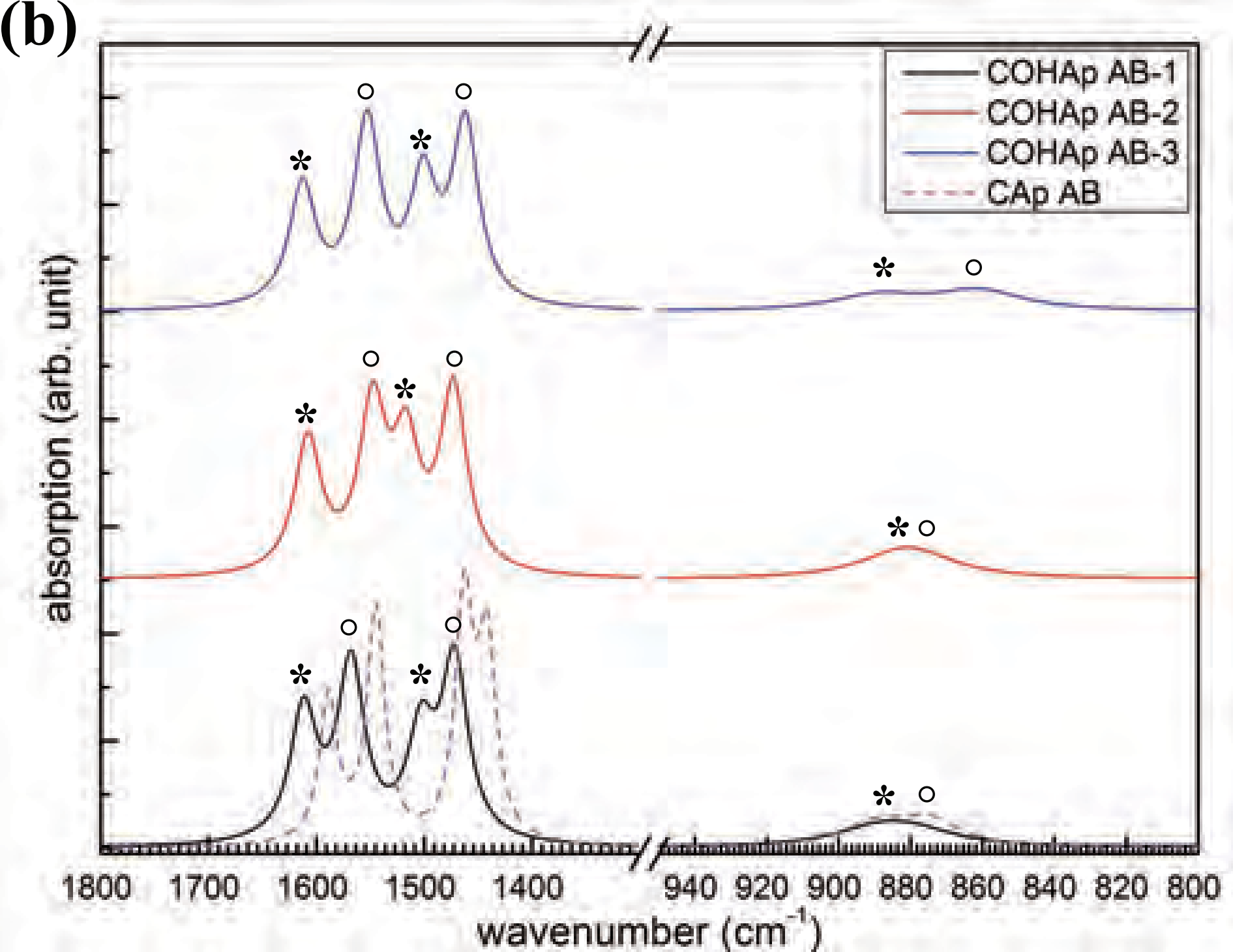
(b)
COHAp AB-1
COHAp AB-2
COHAp AB-3
CAp AB
absorption (arb. unit)
1800 1700 1600 1500 1400 940 920 900 880 860 840 820 800
wavenumber (cm^{-1})